Journal of Materials Chemistry C

ROYAL SOCIETY OF CHEMISTRY

PAPER

View Article Online
View Journal | View Issue

Cite this: J. Mater. Chem. C, 2024, 12, 4273

Evaluation of acenes as potential acceptors in thermally activated delayed fluorescence emitters and the promise of a phenoxazine–naphthalene emitter for OLEDs†‡

Oliver S. Lee, [ab] Nidhi Sharma,[ab] Tomas Matulaitis, [a] Alexandra M. Z. Slawin, [a] Yoann Olivier, [c] Ifor D. W. Samuel, [b] Malte C. Gather *[bd] and Eli Zysman-Colman *[a]

Received 21st November 2023,
Accepted 16th January 2024

DOI: 10.1039/d3tc04292h

rsc.li/materials-c

Thermally activated delayed fluorescence (TADF) is one of the most promising technologies for harvesting triplet excitons in all-organic emitters, a property that is essential for achieving high efficiency in devices. Compounds that operate *via* this mechanism for emission typically rely on a combination of electron donating and accepting moieties separated by an aromatic bridge. Here we demonstrate that although naphthalene is underutilised as an acceptor, it can nonetheless be used in a donor–acceptor TADF emitter when coupled to two phenoxazines in the 1- and 4-positions. The compound **1,4-PXZ-Nap-PXZ** emits at 508 nm, has a photoluminescence quantum yield of 48% and a delayed lifetime of 22.7 ms in a 20 wt% doped film in 1,3-bis(*N*-carbazolyl)benzene (mCP). An organic light-emitting diode (OLED) using this emitter showed a maximum external quantum efficiency (EQE_{max}) of 11% and green emission at λ_{EL} of 505 nm, demonstrating for the first time the potential of naphthalene-acceptor based emitters for devices. Finally, we have demonstrated by way of a density functional theory (DFT) study why naphthalene alone amongst linear acenes is suitable for this role.

Introduction

Of the various competing display technologies used in the modern world, that of the organic light-emitting diode (OLED) is rapidly becoming one of the most widely adopted. This is because OLEDs offer numerous advantages over other display technologies, including high efficiencies, the capacity to view the display at wide angle without loss of image quality, improved contrast, faster refresh rate and an access to a multitude of form factors. In particular, OLEDs can be integrated into flexible and foldable displays and lighting panels, something that is not possible with other display technologies.[1] In an OLED, light is generated by the radiative decay of an exciton that forms following electrical excitation of an emitting molecule, which can be, for instance, an organic (or organometallic) small-molecule or polymer that is located centrally in a stack of organic semiconducting layers sandwiched between two electrodes.[1,2] The overall efficiency of an OLED is quantified in terms of its external quantum efficiency (EQE), which relates to the ratio of supplied electrons to observed photons.

$$EQE = \gamma \cdot n_{ST} \cdot \Phi_{PL} \cdot n_{out} \quad (1)$$

EQE is the product of four terms (eqn (1)),[3] the most important of which for emitter design is the exciton utilization efficiency (n_{ST}), the ratio of generated excitons that can undergo allowed radiative transitions to the ground state. This is because the charge carrier balance (γ) and photoluminescence quantum yield (PLQY, Φ_{PL}) can both equal unity in an optimally functioning device,[1] while the outcoupling efficiency (n_{out}) is typically limited to only 20% as the transition dipole moments of the emitter molecules are distributed isotropically.[4] Meanwhile, n_{ST} depends on the mechanism of emission, because under electrical excitation excitons are generated through hole

[a] Organic Semiconductor Centre, EaStCHEM School of Chemistry, University of St Andrews, St Andrews, KY16 9ST, UK. E-mail: eli.zysman-colman@st-andrews.ac.uk
[b] Organic Semiconductor Centre, SUPA School of Physics and Astronomy, University of St Andrews, St Andrews, KY16 9SS, UK
[c] Laboratory for Chemistry of Novel Materials, University of Mons-Hainaut, Place du Parc 20, B-7000 Mons, Belgium
[d] Humboldt Centre for Nano- and Biophotonics, Department of Chemistry, University of Cologne, Greinstr. 4-6, 50939 Köln, Germany. E-mail: malte.gather@uni-koeln.de

† Electronic supplementary information (ESI) available: ^{1}H NMR and ^{13}C NMR spectra, GCMS, HRMS and reverse phase HPLC; supplementary computational data and coordinates; crystallographic data (CIF). Additional photophysical and OLED data. CCDC 2303516–2303518. For ESI and crystallographic data in CIF or other electronic format see DOI: https://doi.org/10.1039/d3tc04292h

‡ The research data underpinning this publication can be accessed at https://doi.org/10.17630/10e31a40-6c9d-4cc4-bffb-02d57683c6f2

and electron recombination in a 75 : 25 ratio of triplets to singlets.[1,3] Thus if a material is only capable of productively harvesting singlet excitons to produce light, as is the case for purely fluorescent emitters, its internal quantum efficiency (IQE; the product of γ, n_{ST} and Φ_{PL}) will be limited to 25%, and its maximum EQE will be limited to around 5%. By contrast, phosphorescent emitters can harvest both singlet and triplet excitons, owing to strong spin–orbit coupling between the excited states which permits singlet to triplet interconversion *via* intersystem crossing (ISC) and reverse intersystem crossing (RISC). These triplet excitons can then radiatively decay *via* phosphorescence, thereby allowing 100% of the generated excitons to emit light. High spin–orbit coupling is normally induced by the inclusion of a heavy metal atom (or atoms) in the emitter, as is the case with organometallic complexes. However, the heavy metals, most commonly Pt and Ir, that these so-called 2nd-generation emitters rely upon have a number of inherent drawbacks, including: uneven distribution across the Earth's crust, low natural abundance compared to the atoms of all-organic emitters and, to a degree, relatively high cost.[5,6] As such, there is still significant demand for materials that emit *via* alternative triplet harvesting mechanisms, and of these the most promising is that of thermally activated delayed fluorescence (TADF). In this mechanism the singlet–triplet splitting energy (ΔE_{ST}) is sufficiently small to permit endothermic upconversion of triplet excitons into singlets *via* RISC.[1,7] If the gap is sufficiently small, this can be achieved even with the modest spin–orbit coupling present in all-organic emitters. These upconverted triplet excitons can then emit from the singlet excited state at the same emission wavelength as the initially generated singlet excitons, but with a longer overall excited state lifetime. This mechanism likewise allows 100% of generated excitons to emit light but without necessitating the inclusion of a heavy metal.

Modern emitter design is frequently aided by *in silico* modelling. Density functional theory (DFT) can predict the energies of both singlet and triplet excited states *via* the time-dependent (TD-)DFT formalism. These calculations are able to predict real-world trends among a series of compounds.[8] Accurate prediction of absolute energies is also possible, but is more challenging to achieve since it requires the proper inclusion of multiple effects such as solvent stabilization, changes in the excited-state geometry, vibronic effects, as well as conformational disorder. In addition to energies, TD-DFT can also calculate the oscillator strength and the nature of the excited sate. The oscillator strength closely relates to the radiative decay rate and thus the Φ_{PL}, and larger values correspond to a more probable transition. Meanwhile, the 'nature' of the excited state indicates which molecular orbitals contribute to the transition, and from the localization of these orbitals around the molecule it is possible to estimate the degree of charge-transfer (CT) or locally-excited (LE) character of the excited state, and which molecular units of the molecule are involved in the electronic transition. DFT can also calculate the energies of the highest occupied and lowest unoccupied molecular orbitals (HOMO and LUMO respectively), which can be used to quantify the strength of the donor and acceptor moieties of the emitter. A more stabilised LUMO and more destabilised HOMO correspond to a stronger acceptor and stronger donor, respectively. Finally, it is also possible to calculate the spin–orbit coupling (SOC, H_{SO}) between two excited states of different spin multiplicities, which in the case of TADF involves a singlet and a triplet excited state. This property indicates the degree of coupling between the two states which thus opens both intersystem and reverse-intersystem crossing pathways, both of prime importance when discussing the TADF mechanism.[1]

TADF emitter design typically targets minimising ΔE_{ST} by localising the hole and the electron densities (for a two-state electronic transition, these usually correspond to the HOMO and LUMO, respectively) of the emitter to a (number of) donor and acceptor moieties. These moieties are then typically linked *via* an aromatic bridge[7] to ensure sufficient overlap between the HOMO and LUMO, which is necessary to maintain a large oscillator strength and thus efficient fluorescence. The most commonly used aromatic bridge is benzene, yet its larger homolog, naphthalene, has been used only rarely.[9–12] This is curious, both because naphthalene is bulkier than benzene and ought to induce larger torsion angles between the donor/acceptor and the central bridge, which is beneficial for reducing ΔE_{ST}, and also because the larger π-system possesses a more stabilised LUMO, opening the possibility of using naphthalene itself as the electron-accepting moiety.

Indeed, of the plethora of OLED emitters, only three notable reports can be found of compounds containing naphthalene (Fig. 1). These are: (1) **1,4-naphthyl-CF$_3$** and **1,5-Naphthyl-CF$_3$**, two fluorescent blue (λ_{EL} = 453 and 446 nm, respectively) donor–bridge–acceptor emitters where naphthalene acts as a bridge[9] that show moderate Φ_{PL} (67 and 36%, respectively) in toluene solution. OLEDs with these emitters show a maximum external quantum efficiency (EQE_{max}) of 2.3% in both cases; (2) a donor–acceptor–donor emitter, **DPTZN**, in which naphthalene acts as the acceptor and that emits *via* room-temperature phosphorescence (RTP).[10] This molecule shows a remarkable enhancement of the RTP when blended with TRZ-BIM at 10 wt% doping, where the Φ_{PL} is 38% compared to only 3% in the neat film. A device based on this blend showed yellow emission (λ_{EL} = 570 nm) with an EQE_{max} of 11.5%; notably, the mechanism underpinning the RTP enhancement was not elucidated by the authors; (3) finally, a donor–bridge–acceptor TADF emitter, **BTaz-Na-PXZ**,[11] which is to the best of our knowledge the first known example of a naphthalene-containing compound showing TADF. This compound exhibits weak, blue emission (λ_{PL} = 473 nm) as the Φ_{PL} = 18% as a 1 wt% doped film in Zeonex; no devices were fabricated. In addition, two further reports document the use of naphthalene-containing compounds as materials used in OLEDs: (1) a fluorescent emitter with the naphthalene moiety attached to the periphery of the structure that likely is not involved in the electronic transition;[13] and (2) two naphthalene-containing molecules used as the charge recombination layer in white OLEDs (WOLEDs), which likewise are not involved directly in the emission.[14]

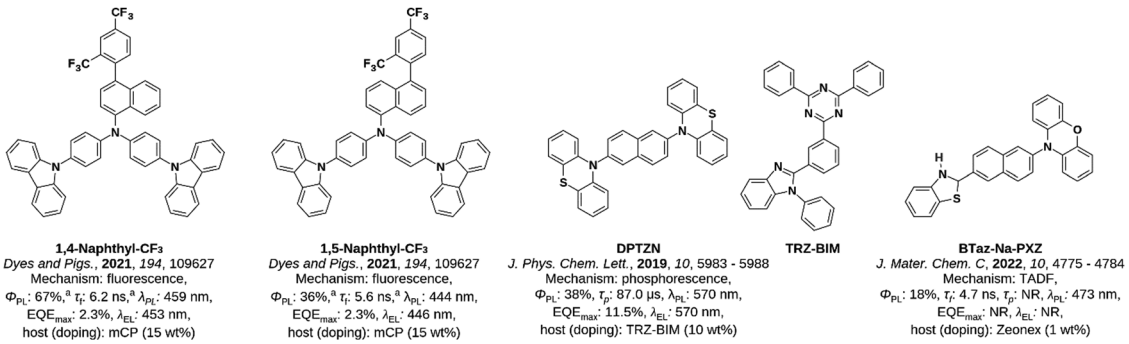

Fig. 1 Structures and photophysical properties of previously reported examples of naphthalene-based emitters. Results are shown for doped films (or doped devices) with the host and doping concentration shown, unless otherwise specified. [a] In degassed toluene solution. NR: not recorded.

Here, we demonstrate the viability of naphthalene-based compounds as emitters in OLEDs where the naphthalene acts as the electron-accepting moiety in a donor–acceptor–donor compound. We additionally demonstrate using density-functional theory (DFT) computations that naphthalene, of all the linear acenes up to hexacene, is ideally suited to act as an acceptor in TADF emitter design.

Computational screen

We initiated a DFT computational screen of 36 naphthalene-based compounds containing one of six different donor moieties with a range of donating strengths and sizes to simultaneously probe the effect of both electronics and sterics. These donors were diphenylamine (DPA), carbazole (Cz), 3,6-di-*tert*-butylcarbazole (DTBCz), 1,8-dimethylcarbazole (DMCz), 9,9-dimethyldihydroacridine (DMAC) and phenoxazine (PXZ). These donors decorate the naphthalene in either the 1-, 1,4-, 2- or 2,6-configurations where in the doubly substituted compounds, the second substituent was either another equivalent of the same donor or alternatively 2,4-diphenyl-1,3,5-triazine (TRZ) (Fig. 2), the latter being a stronger acceptor than naphthalene and serving to further stabilise the LUMO of the emitter.

The full results from this investigation are available in the ESI† (Table S1). In summary, four of the compounds, **1-PXZ-Nap**, **1,4-PXZ-Nap-PXZ**, **2-PXZ-Nap** and **2,6-PXZ-Nap-PXZ** were identified as having the most promising traits to show TADF. Crucially, each of these four compounds were computed to have a ΔE_{ST} of below 0.1 eV. The analogous structures **1,4-PXZ-Nap-TRZ** and **2,6-PXZ-Nap-TRZ** have similarly small ΔE_{ST}, but the stronger TRZ acceptor further stabilises the S_1 energy to 2.20 and 2.34 eV, respectively. As blue-emitting OLEDs are typically in higher demand than green or yellow emitting, we chose to target the higher energy compounds. A marginally higher ΔE_{ST} was calculated for **2-PXZ-Nap** and **2,6-PXZ-Nap-PXZ** of 0.06 and 0.04 eV, respectively, compared to 0.01 eV for each of **1-PXZ-Nap** and **1,4-PXZ-Nap-PXZ**. However, in the compounds with a larger ΔE_{ST}, the H_{SO} was also larger, at 0.24 and 0.15 cm^{-1} for **2-PXZ-Nap**, **2,6-PXZ-Nap-PXZ**, respectively, compared to 0.03 and <0.01 cm^{-1} for **1-PXZ-Nap** and **1,4-PXZ-Nap-PXZ**, respectively. This competing effect between diminishing ΔE_{ST} and maintaining SOC has been described previously in the literature.[16] Hence, three of the four emitters have an effectively equivalent first-order mixing coefficient of around 10^{-4}, with only **1,4-PXZ-Nap-PXZ** having a significantly smaller mixing coefficient of around 10^{-6} due to the much

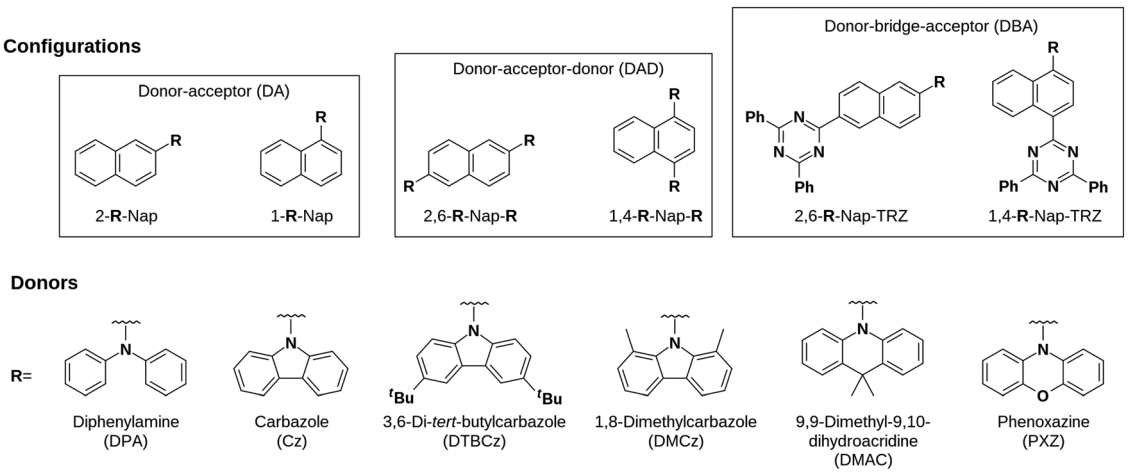

Fig. 2 General structures of the 36 compounds investigated computationally.

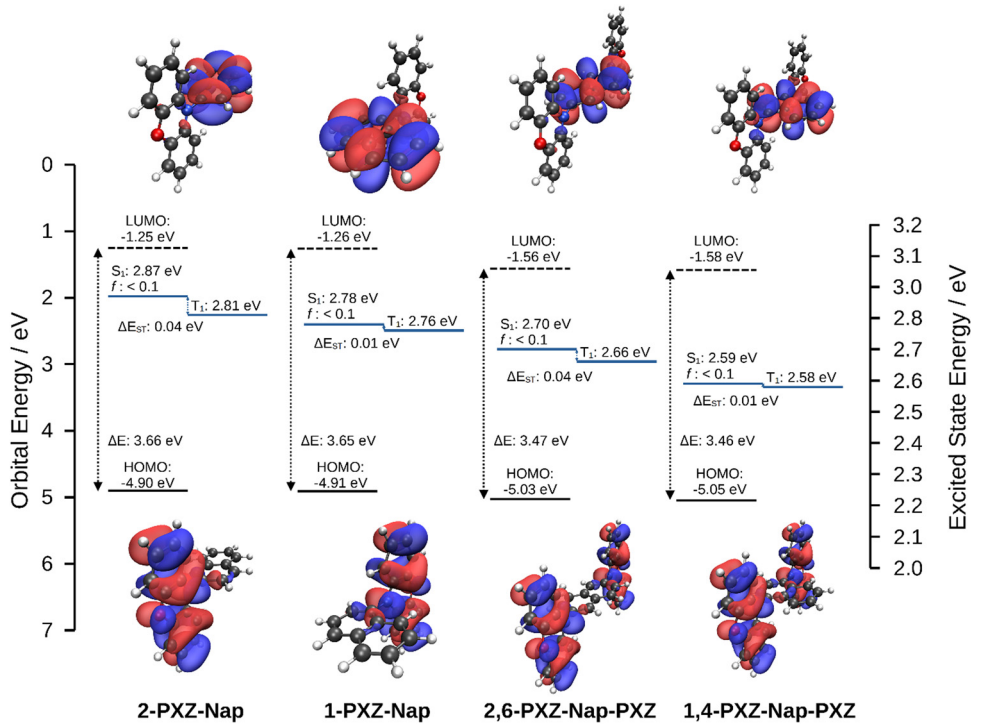

Fig. 3 Computed HOMO & LUMO energies with associated densities (isovalue = 0.02) as computed at the PBE0-D3(BJ)/6-31G(d,p) level of theory and excited state energies, calculated at the TDA-PBE0-D3(BJ)/6-31G(d,p) level of theory in the gas phase.

smaller H_{SO} in this emitter. This highlights that the S_1 and T_1 excited states remain largely pure spin states. In all cases, the small ΔE_{ST} values can be attributed to excellent confinement of the HOMO and LUMO onto the PXZ donor and naphthalene acceptor moieties, respectively, as evidenced from the orbital distributions of the DFT-optimised structures (Fig. 3). In turn, this localization is the result of the large torsion angles between the donor(s) and acceptor, which is close to perpendicular in all cases, and, to a lesser extent, the high donating strength of the PXZ moiety, as reflected by the computed HOMO energies. The four molecules have a predicted S_1 excitation energy ranging from 433 nm for **2-PXZ-Nap** to 479 nm for **1,4-PXZ-Nap-PXZ**. This trend is naturally mirrored in the calculated HOMO–LUMO gap ($\Delta E_{HOMO-LUMO}$), being largest in **2-PXZ-Nap** (3.66 eV) and decreasing to 3.46 eV in **1,4-PXZ-Nap-PXZ** since the S_1 excited states of all molecules are dominated by a HOMO to LUMO transition. As might be expected, the largest change in both the S_1 energy and $\Delta E_{HOMO-LUMO}$ was observed between the singly and doubly donor-substituted examples; however, this change was driven primarily by a stabilisation of the LUMO level as opposed to a destabilisation of the HOMO, despite the addition of a second donor unit. Finally, in all cases the predicted oscillator strength for the $S_0 \rightarrow S_1$ transition is negligible. However, this is typical in charge-transfer type emitters such as those investigated here, in which the HOMO–LUMO overlap in the ground state-optimised structure is intentionally minimised and the probability of the transition becomes small.[17] These emitters can still possess high efficiencies in the real world so long as emission of the S_1 is coupled to vibrational modes inducing either: (1) a reduced donor–acceptor torsion and hence greater HOMO–LUMO overlap or (2) contributions from electronic transitions between deeper occupied molecular orbitals and higher-lying unoccupied molecular orbitals.[18]

Synthesis

Based on the theoretical study, we next targeted the synthesis of the four compounds. **1-PXZ-Nap**, **2-PXZ-Nap** and **1,4-PXZ-Nap-PXZ** were each obtained following a Pd-catalysed Buchwald–Hartwig cross-coupling reaction of the relevant mono or di-halogenated naphthalene and phenoxazine in 34%, 56% and 31% yield, respectively (Schemes S3–S5, ESI†). Surprisingly, **2,6-PXZ-Nap-PXZ** could not be obtained by this route and thus this target was abandoned at this stage for further investigation. We also note that the mono-substituted product from the reaction of 1,4-dibromonaphthalene and phenoxazine, 1-bromo-4-phenoxylnaphthalene, could not be isolated, regardless of the stoichiometry of phenoxazine used. The synthesised emitters were fully characterised by ^{1}H and ^{13}C nuclear magnetic resonance (NMR) spectroscopy, gas-chromatography/mass-spectrometry (GCMS), high-pressure liquid chromatography (HPLC), melting point analysis, and structure elucidation by single-crystal X-ray diffraction. Full synthetic details are available in the ESI.†

Crystal structures

The structures of each of the three emitters were determined by single crystal X-ray crystallography. Each of the crystals was

grown by vapour diffusion of hexane into toluene. These structures are shown in Fig. 4; in all three compounds the central naphthalene is planar while the phenoxazine donor is puckered around the connecting nitrogen atom. In the related **1-PXZ-Nap** and **1,4-PXZ-Nap-PXZ** structures, there is a close to perpendicular dihedral angle between the phenoxazine and naphthalene groups of 82.3° and 82.0°, respectively, while the less sterically hindered **2-PXZ-Nap** has a more relaxed dihedral angle of 72.0°. The difference in geometry between the **1-PXZ-Nap**/**1,4-PXZ-Nap-PXZ** and **2-PXZ-Nap** agrees with the trend predicted by DFT (Table 1). A complete analysis of the obtained crystal structures is available in the ESI† (S6).

Electrochemistry

Cyclic (CV) and differential pulse (DPV) voltammograms for each of the three synthesised emitters were recorded in acetonitrile and are shown in Fig. 5 and the electrochemical data are collated in Table 2. Clear and reversible oxidation and reduction waves are observed for each of **2-PXZ-Nap**, **1-PXZ-Nap** and **1,4-PXZ-Nap-PXZ**, corresponding to estimated HOMO/LUMO values of −5.08/−3.52, −5.12/−3.53 and −5.13/−3.52 eV, respectively. The LUMO energy shows essentially no variance with emitter structure, which is to be expected considering how electronically decoupled the donor PXZ groups are with the naphthalene acceptor. There is also little variation in the HOMO energy, even between **1-PXZ-Nap** and **1,4-PXZ-Nap-PXZ**. The corresponding HOMO–LUMO gaps are 1.56, 1.59 and 1.61 eV for **2-PXZ-Nap**, **1-PXZ-Nap** and **1,4-PXZ-Nap-PXZ**, respectively. Compared to the naphthalene-based emitters that have been previously reported,[9,10] the HOMO energies of these three emitters are generally more destabilised while the LUMO energies are notably more stabilised. As such, the HOMO–LUMO gaps are smaller at *ca.* 1.6 eV, compared to *ca.* 3.0, 3.0 and 2.7 eV for **1,4-naphthyl-CF$_3$**,[9] **1,5-naphthyl-CF$_3$**,[9] and **DPTZN**,[10] respectively (Table 2). Finally, the trend in the measured HOMO/LUMO energies matches that predicted by DFT, although the absolute energies of the LUMO are more stabilised than the predictions.

Absorption and photoluminescence

Absorption (Abs) and photoluminescence (PL) spectra for each of the three emitters were recorded in dilute toluene solution (Fig. 6a). Each emitter shows an intense and structured absorption band centred around *ca.* 300 nm corresponding to the overlap of peaks from the local excitation (LE) of both the central naphthalene moiety[20] and the terminal phenoxazine donor.[21] The contribution of the phenoxazine moiety is clearly demonstrated by the increase in molar absorptivity of this LE band in the doubly substituted **1,4-PXZ-Nap-PXZ** compared to either of the singly substituted emitters. In addition, an unstructured and less intense band can be observed that is red-shifted relative to the LE band in all three compounds, appearing as a shoulder in **2-PXZ-Nap** and **1-PXZ-Nap** at *ca.* 375 nm and as a distinct band in **1,4-PXZ-Nap-PXZ** at 402 nm. This lower energy band is assigned to the charge transfer (CT) transition between the phenoxazine donor and naphthalene acceptor and is noticeably more intense in the doubly substituted **1,4-PXZ-Nap-PXZ**. This arises because the second equivalent of the phenoxazine donor moiety increases the overlap between the HOMO and LUMO, thus increasing the probability of transition. As well, the CT absorption band is red-shifted in **1,4-PXZ-Nap-PXZ** compared to the singly substituted emitters as the HOMO is destabilized due to the presence of the second electron-donating PXZ. The observed trend in the CT band absorption energies mirrors the S_1 energies predicted by TDA-DFT; however, the molar absorptivities do not, where the predicted oscillator strength, *f*, of the $S_0 \rightarrow S_1$ transition at

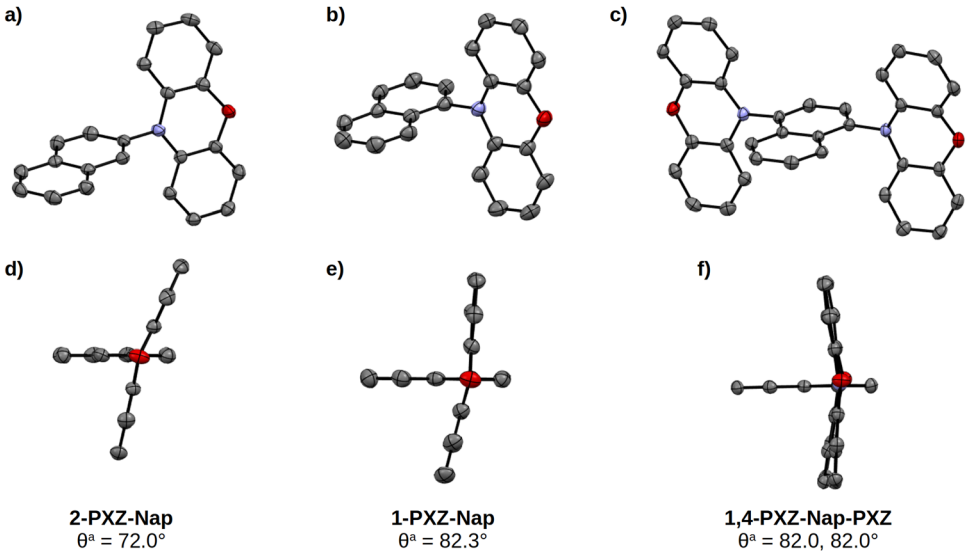

Fig. 4 Structures of **2-PXZ-Nap** (a) and (d), **1-PXZ-Nap** (b) and (e) and **1,4-PXZ-Nap-PXZ** (c) and (f) derived from single-crystal X-ray crystallography. Atoms are shown as thermal ellipsoids at the 50% probability level. Hydrogen atoms have been omitted for clarity. [a] Dihedral angle between donor and acceptor moieties, measured as the average of the four absolute dihedral angles between the two groups where angles >180° have been normalised according to the formula $\theta_{norm} = \theta - 180$.

Table 1 Computational results computed at the TDA-PBE0-D3(BJ)/6-31G(d,p) level of theory

Structure	E_{S_1}[a]/eV (nm)	f_{S_1}[b]	ΔE_{ST}[c]/eV	H_{SO}[d]/cm^{-1}	$H_{SO}/\Delta E_{ST}$[e]	E_{HOMO}/eV	E_{LUMO}/eV	θ[f]/°
2-PXZ-Nap	2.87 (433)	<0.01	0.06	0.24	5.27×10^{-4}	−4.90	−1.25	80.7
1-PXZ-Nap	2.78 (447)	<0.01	0.01	0.03	2.83×10^{-4}	−4.91	−1.26	83.2
2,6-PXZ-Nap-PXZ	2.70 (459)	<0.01	0.04	0.15	4.79×10^{-4}	−5.03	−1.56	80.4, 80.4
1,4-PXZ-Nap-PXZ	2.59 (479)	<0.01	0.01	<0.01	9.76×10^{-7}	−5.05	−1.58	82.8, 82.8

[a] Energy of the first singlet excited state. [b] Oscillator strength of the $S_0 \rightarrow S_1$ transition. [c] S_1–T_1 energy gap. [d] Spin–orbit coupling between S_1 and T_1 at the ground state geometry, calculated using the PySOC program.[15] [e] First-order mixing coefficient between S_1 and T_1.[f] Dihedral angle between the donor and acceptor moieties, measured as the average of the four absolute dihedral angles between the two groups where angles >180° have been normalised according to the formula $\theta_{norm} = \theta - 180$.

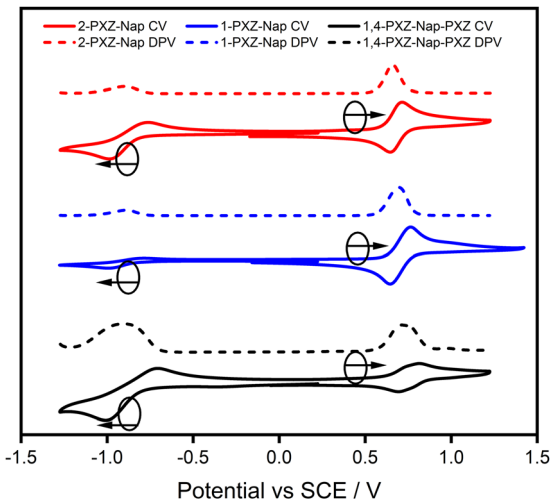

Fig. 5 Cyclic and differential pulse voltammograms for the emitters **2-PXZ-Nap**, **1-PXZ-Nap** and **1,4-PXZ-Nap-PXZ**, measured in acetonitrile and referenced to a saturated calomel electrode (0.45 V *vs.* SCE[19]) with a scan rate of 0.1 V s^{-1}.

the optimised geometries for each of the emitters is *ca.* 0, as at this geometry there is a near orthogonal conformation between the donor and acceptor groups. The PL spectrum of each emitter shows a single, unstructured band peaking at λ_{PL} = 455, 476 and 496 nm for **2-PXZ-Nap**, **1-PXZ-Nap** and **1,4-PXZ-Nap-PXZ**, respectively, reflecting emission from a CT state. The corresponding Stokes shifts are 80, 101 and 94 nm (4687, 5614 and 4714 cm^{-1}), respectively, relative to the CT absorption band. In contrast to the absorption spectra, which show little variation with structure, a clear trend can be seen with the λ_{PL} values, with **2-PXZ-Nap** emitting in the deep blue, followed by **1-PXZ-Nap** and then **1,4-PXZ-Nap-PXZ** emitting in the sky-blue regime. In particular, the difference between the two singly substituted structures demonstrates that the emission energy of this class of donor-naphthalene type emitters is influenced not only by the number of donors but also their substitution pattern around the naphthalene ring. We hypothesise that the apparent difference in behaviour of the CT absorption band and the CT emission band in relation to molecular structure is caused by the CT absorption band being partially masked by the much larger LE absorption band, which makes its peak position difficult to ascertain accurately. TDA-DFT calculations at the relaxed excited state of all three emitters show an equivalent stabilisation of *ca.* 0.56 eV (Table S3, ESI†) compared to the vertical excited state. We thus conclude that there is no increased stabilisation of the conformation of **2-PXZ-Nap** in the relaxed excited state that is responsible for its apparent reduced Stokes shift compared to **1-PXZ-Nap**.

We then proceeded to investigate the photophysical properties of each of the emitters in greater detail in solution (Table 3). In toluene, the time-resolved PL decays of both of the singly substituted emitters exhibited a single decay process with comparable lifetimes, τ_p, of 2.8 and 3.1 ns for **2-PXZ-Nap** and **1-PXZ-Nap**, respectively, indicating that the origin of the emission is fluorescence. By contrast, the τ_p of **1,4-PXZ-Nap-PXZ** is approximately double at 6.4 ns. No delayed lifetime was observed for any of the three compounds in toluene. In dichloromethane, the λ_{PL} of each emitter was red-shifted relative to toluene (Fig. 6b) to λ_{PL} = 502, 518 and 536 nm for **2-PXZ-Nap**, **1-PXZ-Nap** and **1,4-PXZ-Nap-PXZ**, respectively. These values correspond to a red-shift of 40–50 nm compared to toluene, and originate from the increased stabilisation of the singlet excited state of the emitters in the more polar DCM.

Table 2 Summary of electrochemical data of the new emitters in this work and literature examples

Emitter	E_{ox}[a]/V	E_{red}[a]/V	E_{HOMO}[b]/eV	E_{LUMO}[b]/eV	$\Delta E_{HOMO-LUMO}$/eV
2-PXZ-Nap	0.28	−1.28	−5.08	−3.52	1.56
1-PXZ-Nap	0.32	−1.27	−5.12	−3.53	1.59
1,4-PXZ-Nap-PXZ	0.33	−1.28	−5.13	−3.52	1.61
1,4-naphthyl-CF$_3$[9]	0.46	NR	−5.24	−2.21[c]	3.03
1,5-naphthyl-CF$_3$[9]	0.45	NR	−5.23	−2.18[c]	3.05
DPTZN[10]	0.55[d]	−2.1[d]	−5.35	−2.70	2.65
BTaz-Ph-PXZ[11]	NR	NR	NR	NR	NR

[a] Oxidation/reduction potentials obtained from the peak of the DPV using Fc/Fc$^+$ as the internal standard and referenced to SCE.[19] [b] Measured from the onset of oxidation/reduction peak. [c] Calculated by the authors as $E_{LUMO} = E_{HOMO} + E_{opt}$, where E_{opt} is the optical gap estimated from UV-vis absorption spectra. [d] Calculated from reported E_{HOMO}/E_{LUMO}, according to $E_{ox} = E_{HOMO} - 4.8$ and $E_{red} = 4.8 - E_{LUMO}$.[11] NR: not recorded.

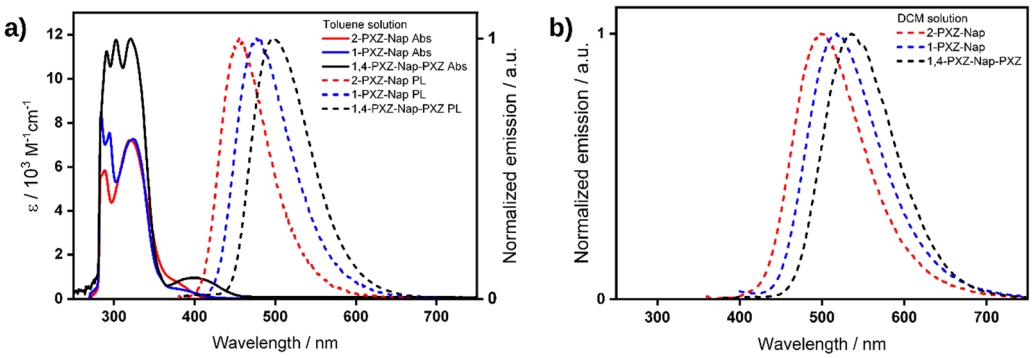

Fig. 6 (a) UV-vis absorption (Abs, solid lines) and photoluminescence (PL, dashed lines) of dilute toluene solutions of **2-PXZ-Nap** (red), **1-PXZ-Nap** (blue) and **1,4-PXZ-Nap-PXZ** (black), λ_{exc} = 322, 340, 325 nm, respectively. (b) PL spectra of dilute dichloromethane solutions of the same, λ_{exc} = 326, 326, 400 nm, respectively.

Table 3 Summary of the photophysical properties of the three emitters in solution

	Toluene			Dichloromethane				2MeTHF
Emitter	λ_{abs}[a]/nm (ε/10³ M⁻¹ cm⁻¹)	λ_{PL}[b]/nm	τ_p[c]/ns	λ_{PL}[a]/nm	Φ_{PL}[b]/%	τ_p[c]/ns	τ_d[c]/μs	ΔE_{ST}/eV
2-PXZ-Nap	375 (0.81)	455	2.8	502	NR	7.5	51.4	0.52
1-PXZ-Nap	375 (0.48)	476	3.1	518	NR	8.0	0.2	0.40
1,4-PXZ-Nap-PXZ	402 (0.83)	496	6.4	536	40 (22)	15.4	148.2	0.24

[a] Estimated from the peak of the measured spectrum. [b] Photoluminescence quantum yield in toluene relative to quinine sulfate in 1 M H_2SO_4 (Φ_{PL} = 54.6%), measured in degassed solution.[22] Value in parentheses is in air. [c] Prompt (τ_p) and delayed (τ_d) lifetime. NR: not recorded. No delayed emission was observed in toluene. Steady-state and time-gated spectra in 2-MeTHF are available in the ESI (Fig. S15). λ_{exc} = 322, 340, 325 nm (toluene λ_{PL}, 2-PXZ-Nap, 1-PXZ-Nap and 1,4-PXZ-Nap-PXZ, respectively), 375 nm (toluene τ_p), 326, 326, 400 nm (DCM λ_{PL}, 2-PXZ-Nap, 1-PXZ-Nap and 1,4-PXZ-Nap-PXZ, respectively), 360 nm (DCM Φ_{PL}), 326, 326, 375 nm (DCM, τ_p and τ_d, 2-PXZ-Nap, 1-PXZ-Nap and 1,4-PXZ-Nap-PXZ, respectively), and 310 nm (2-MeTHF ΔE_{ST}).

In comparison to toluene, each emitter in DCM exhibited two distinct decay processes with the same emission maxima (Fig. 7), with prompt lifetimes τ_p, of 7.5, 8.0 and 15.4 ns, and delayed lifetimes, τ_d, of 51.4, 0.2 and 148.2 μs, for **2-PXZ-Nap**, **1-PXZ-Nap** and **1,4-PXZ-Nap-PXZ** respectively. The prompt lifetimes retain the same pattern as was observed in toluene, with the singly substituted emitters decaying roughly twice as quickly as the doubly substituted. However, all three decays were slower in DCM than in toluene which is consistent with an overall increase of the CT character of the first singlet excited state in the more polar solvent. By contrast, the delayed lifetimes show a much greater dependence on substitution pattern, spanning four orders of magnitude from **1-PXZ-Nap** (219 ns) to **1,4-PXZ-Nap-PXZ** (148 μs), although the decays of the two singly substituted emitters remain faster than that of the doubly substituted, as was observed in toluene. In addition to having a shorter lifetime, the delayed fluorescence of **1-PXZ-Nap** and **2-PXZ-Nap** was also significantly weaker than that of **1,4-PXZ-Nap-PXZ**, as evidenced by their respective decay curves (Fig. 7). The delayed emission in all three emitters is biexponential, indicating contribution from multiple emissive states, and the ratio of the two delayed processes is smaller in **1-PXZ-Nap** and **2-PXZ-Nap** than in **1,4-PXZ-Nap-PXZ** (τ_1 : τ_2 = 50 : 50, 10 : 90 and 7 : 93, respectively). Considering the large dihedral angle between the phenoxazine and naphthalene, and the puckering of the phenoxazine moiety observed in the crystal structure (Fig. 4), we hypothesize that the multiple lifetimes originate from different conformers. The Φ_{PL} of **1,4-PXZ-Nap-PXZ** is 40% in degassed DCM solution, compared to only 22% in aerated DCM, indicating a significant contribution from triplet excited states. Owing to the poor Φ_{PL} recorded in the film state (see below), the Φ_{PL} of **2-PXZ-Nap** and **1-PXZ-Nap** were not measured in DCM.

In 2-methyltetrahydrofuran (2-MeTHF), large ΔE_{ST} of 0.52 and 0.40 eV were recorded for **2-PXZ-Nap** and **1-PXZ-Nap**, respectively. These large singlet–triplet gaps result in very sluggish triplet to singlet up-conversion and are the cause of the low delayed emission intensity observed in Fig. 7b and c. By comparison, **1,4-PXZ-Nap-PXZ** has a significantly smaller ΔE_{ST} of 0.24 eV, which results in more efficient RISC, and as such exhibits a greater proportion of delayed emission (Fig. 7d). None of the experimentally obtained ΔE_{ST} values correspond well to the DFT predicted values, which all approach zero. This likely suggests that the geometrically relaxed structures that have approximately orthogonally linked donor and acceptor groups, as observed both computationally and in the crystal structures, are not the predominantly emissive species in 2-MeTHF glass. This is to be expected, considering the *ca.* 0 oscillator strength predicted for the orthogonal structures. Further, DFT computations reveal an equally small ΔE_{ST} and approximately equivalent H_{SO} in both DCM and toluene (Table S4, ESI†), and so differences in the RISC rate of these structures are unlikely to explain the switching on of the delayed emission in DCM

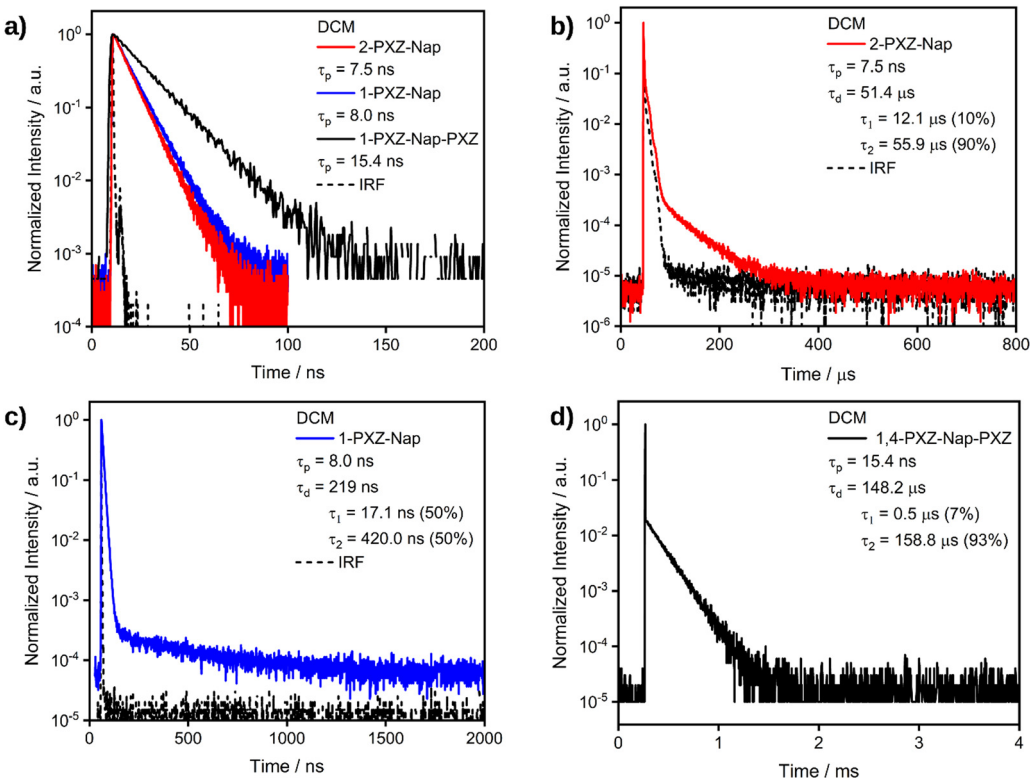

Fig. 7 (a) TRPL of the prompt decay process of **2-PXZ-Nap-PXZ**, **1-PXZ-Nap-PXZ** and **1,4-PXZ-Nap-PXZ**. (b) TRPL of the delayed decay process of **2-PXZ-Nap**. (c) TRPL of the delayed decay process of **1-PXZ-Nap**. (d) TRPL of the delayed decay process of **1,4-PXZ-Nap-PXZ**. Measured in dilute DCM solutions with λ_{exc}: 375 nm in all cases.

only. We instead suggest that non-radiative decay from T_1 is relatively much more suppressed in DCM.

We next investigated the photophysical properties in the solid state. In spin-coated 10 wt% doped films using polymethylmethacrylate (PMMA) as a host, the PL is slightly blue-shifted compared to that in toluene at λ_{PL} of 441, 462 and 491 nm for **2-PXZ-Nap**, **1-PXZ-Nap** and **1,4-PXZ-Nap-PXZ**, respectively (Table 4). The trend in λ_{PL} between the three emitters, however, remained the same as in toluene. The photoluminescence quantum yields, Φ_{PL}, are very low for the two singly substituted emitters at *ca* 2% but is notably higher in **1,4-PXZ-Nap-PXZ** at 22%, which decreases to 18% upon exposure to air. Time-resolved PL of the films revealed the same pattern as was observed in toluene (Fig. 8), with a rapid and broadly equivalent τ_p of 2.9 and 3.6 ns for **2-PXZ-Nap** and **1-PXZ-Nap**, respectively, and a longer τ_p of 11.7 ns for **1,4-PXZ-Nap-PXZ**. The τ_d of **1,4-PXZ-Nap-PXZ** film is 8.0 μs, significantly faster than the 148.2 μs observed in dilute DCM solution, and retains the biexponential character. Compared to DCM, the ratio of the two delayed lifetimes is much small at 33 : 67, indicating a greater contribution to the emission from multiple emissive states. This is typical of emission from doped glassy films, in which the emitter is partially frozen in multiple different conformations, resulting in varying emission lifetimes.[23–25] Neither of the singly substituted emitters demonstrated any delayed emission in the film state.

The PL spectra were then measured in an OLED relevant host of suitably high triplet energy, 1,3-bis(*N*-carbazolyl)-benzene (mCP) at 10 wt% doping concentration. The Φ_{PL} increased to 7% for each of **2-PXZ-Nap**, **1-PXZ-Nap** and 32% for **1,4-PXZ-Nap-PXZ**. There is also a clear decrease in the Φ_{PL} in air, implying that available triplet excited states are being

Table 4 Summary of the photophysical properties of the three emitters in doped films

	10 wt% in PMMA				10 wt% in mCP	20 wt% in mCP			
Emitter	λ_{PL}[ab]/nm	Φ_{PL}[b]/%	τ_p[b]/ns	τ_d[b]/μs	Φ_{PL}/%	λ_{PL}[ab]/nm	Φ_{PL}/%	τ_p[b]/ns	τ_d[b]/μs
2-PXZ-Nap	441	<1 (2)	2.9	—[c]	7 (2)	NR	NR	NR	NR
1-PXZ-Nap	462	2 (1)	3.6	—[c]	7 (2)	NR	NR	NR	NR
1,4-PXZ-Nap-PXZ	491	22 (18)	11.7	8.0	32 (7)	508	48 (7)	88.2	22.7×10^3

[a] Estimated from the peak of the measured spectrum. [b] Measured under vacuum. Values in parentheses are in air. Φ_{PL} values measured using an integrating sphere. [c] Not observed. NR: not recorded. PMMA: polymethylmethacrylate, mCP: 1,3-bis(*N*-carbazolyl)benzene. λ_{exc} = 340, 340, 360 nm (PMMA λ_{PL} and Φ_{PL}, 10 wt% mCP; 2-PXZ-Nap, 1-PXZ-Nap and 1,4-PXZ-Nap-PXZ respectively), 375 nm (PMMA τ_p and τ_d) and 340 nm (20 wt% mCP).

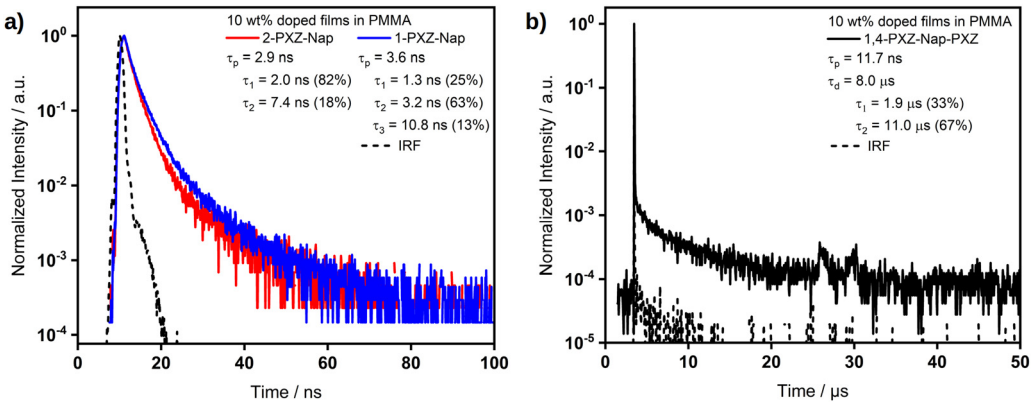

Fig. 8 (a) TRPL of **2-PXZ-Nap** and **1-PXZ-Nap** in 10 wt% doped films in PMMA measured by time-correlated single photon counting (TCSPC), λ_{exc}: 375 nm. (b) TRPL of **1,4-PXZ-Nap-PXZ** in 10 wt% doped films in PMMA measured by time-correlated single photon counting (TCSPC), in λ_{exc}: 375 nm. The data points at *ca.* 25 and 30 μs are an artefact of the measurement process.

quenched by oxygen, down to 7% for **1,4-PXZ-Nap-PXZ** and 2% for both **2-PXZ-Nap** and **1-PXZ-Nap**, although in the latter case the change in Φ_{PL} is close to the measurement error of ±5%.[22] Upon increasing the doping concentration to 20 wt%, the Φ_{PL} of the **1,4-PXZ-Nap-PXZ** film increased to 48%, which is the highest Φ_{PL} we recorded for this emitter. A full doping screen for the three emitters is available in the ESI† (Table S5). In the 20 wt% mCP film, the λ_{PL} red-shifted by 17 nm to 508 nm (Fig. 9) compared to the 10 wt% PMMA, likely owing to increased contribution to the emission from aggregates at the higher doping concentration. Temperature-dependent time-resolved PL decay measurements of the 20 wt% mCP film are shown in Fig. 10. As the temperature increases, the initial proportion of delayed emission also increases (Fig. 10b), which is consistent with a thermally activated pathway in which there is more energy available to upconvert triplets to singlets. The emission lifetime of **1,4-PXZ-Nap-PXZ** also decreases at higher temperature, as evidenced from the steeper slope (Fig. 10a), indicating a faster decay process. This is caused by increased rates of both RISC and non-radiative decay. Finally, the total proportion of delayed emission appears to decrease at elevated temperature. This is caused by the increase in non-radiative decay, which competes with triplet up-conversion and results in reduced delayed emission at long emission times. In considering **2-PXZ-Nap** and **1-PXZ-Nap**, we note that: (1) TDA-DFT calculations predicted a similarly small ΔE_{ST} for the two singly-substituted emitters as the doubly substituted emitter; (2) the measured Φ_{PL} of the films was extremely low, even under vacuum; (3) the delayed lifetime in solution was extremely short. We therefore contend that the absence of TADF in the film state of **2PXZ-Nap** and **1-PXZ-Nap** is largely driven by quenching of the triplet states through non-radiative decay pathways, which simultaneously explains the low Φ_{PL} and short/absent delayed emission.

Electroluminescent (EL) device

As only **1,4-PXZ-Nap-PXZ** was identified as showing TADF in the film state, we only assessed the potential of this compound as an emitter in an OLED. The optimized device structure used was ITO/*N*,*N*′-di(1-naphthyl)-*N*,*N*′-diphenyl-(1,1′-biphenyl)-4,4′-diamine (NPB) (30 nm)/tris(4-carbazoyl-9-ylphenyl)amine (TCTA) (20 nm)/20 wt% **1,4-PXZ-Nap-PXZ** in mCP (20 nm)/2,8-bis-(diphenyl-phosphoryl)-dibenzo[b,d]thiophene (PPT) (10 nm)/1,3,5-tris(3-pyridyl-3-phenyl)benzene (TmPyPB) (40 nm)/LiF (1 nm)/Al (100 nm). The electroluminescence (EL) spectrum of this device along with the recorded efficiency data are presented

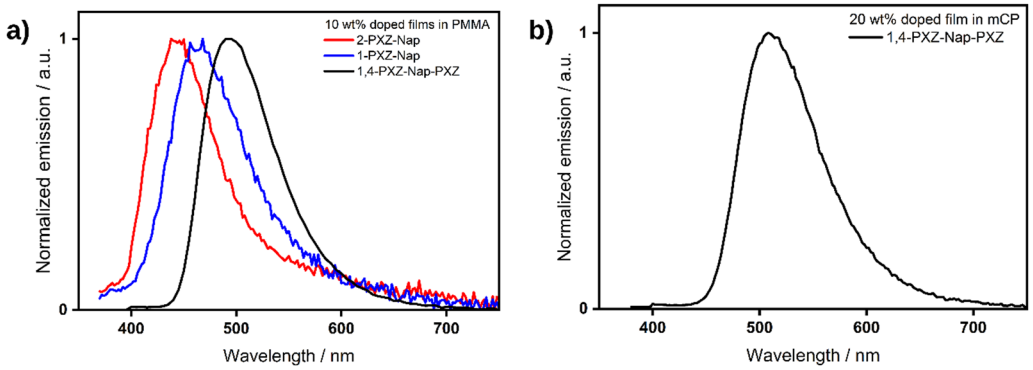

Fig. 9 (a) PL spectra of 10 wt% doped PMMA films of **2-PXZ-Nap** (red), **1-PXZ-Nap** (blue) and **1,4-PXZ-Nap-PXZ** (black), λ_{exc} = 340, 340, 360 nm, respectively. (b) PL of **1,4-PXZ-Nap-PXZ** in 20 wt% mCP doped film. λ_{exc}: 340 nm.

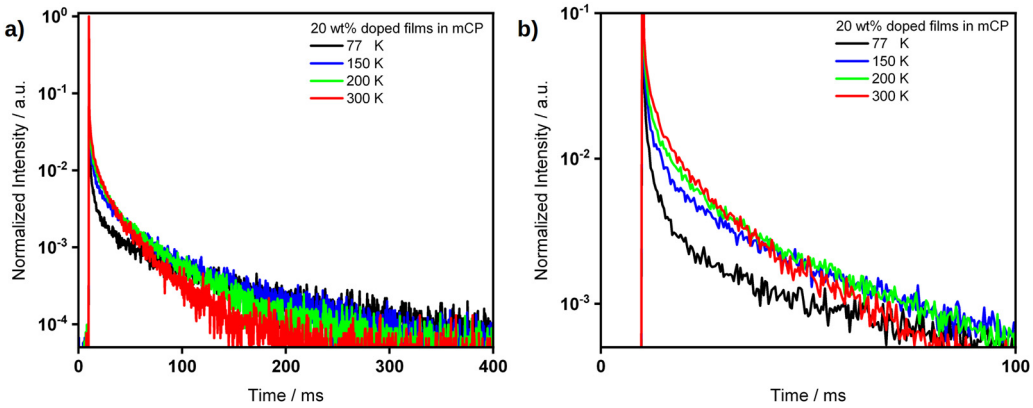

Fig. 10 (a) Temperature-dependent TRPL of the 20 wt% film of **1,4-PXZ-Nap-PXZ** in mCP. (b) Inset of the same. λ_{exc}: 375 nm.

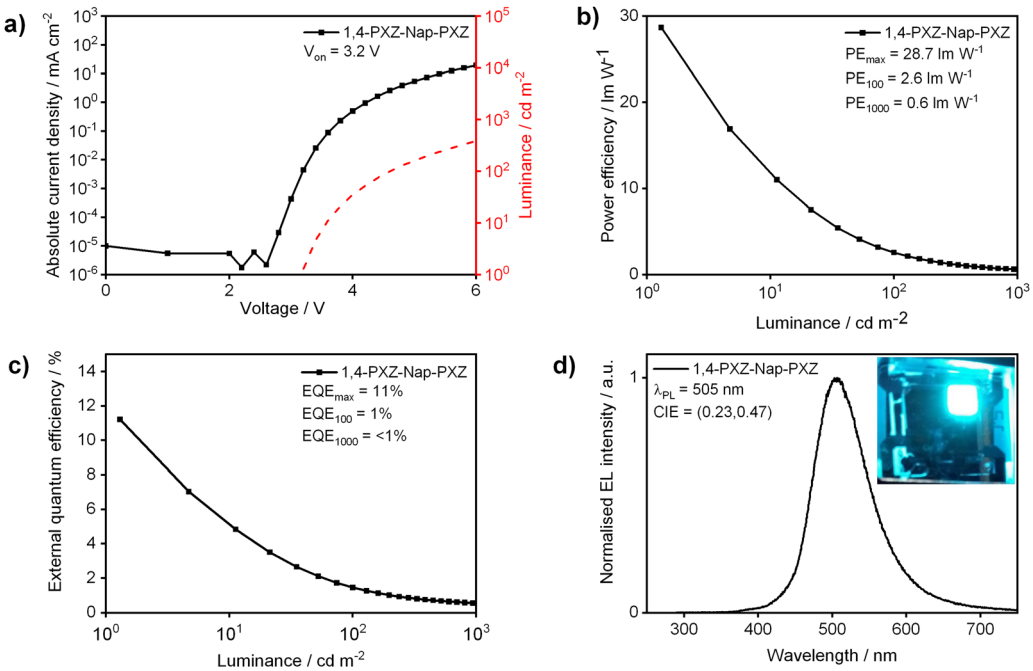

Fig. 11 Electroluminescence spectrum and efficiency data of the OLED.

in Fig. 11. The EL peak, λ_{EL}, at 505 nm is blue-shifted by 3 nm compared to the PL of the 20 wt% mCP film, corresponding to Commission Internationale de l'Éclairage (CIE) coordinates of (0.23, 0.47). The peak external quantum efficiency (EQE_{max}) is 11.2%, clearly more than the 5% theoretical limit for fluorescent OLEDs. Assuming Lambertian emission and values of γ = 1.0, n_{out} = 0.2 and using the measured Φ_{PL} of 48%, this EQE_{max} is larger than the theoretical maximum of 9.6%, assuming isotropic alignment of the transition dipole moment (TDM). This suggests that there is enhanced outcoupling efficiency of the device,[4] implying a degree of preferential horizontal alignment of the TDM of the emitter in the film state. The EQE decreases relatively severely at higher luminance, approaching 1% at 100 cd m^{-2}. Considering the long-delayed lifetime of 22.7 ms and the high doping concentration of the 20 wt% doped film in mCP, this efficiency roll-off is likely caused by the accumulation of triplets leading to emission degradation *via* triplet–triplet annihilation and/or triplet–polaron quenching. Future devices may be able to mitigate this issue through optimisation, particularly by either using a host that promotes a faster delayed emission or that uses a lower emitter doping concentration. To the best of our knowledge, this is the first demonstrated TADF OLED utilising a naphthalene-based emitter. The turn-on voltage (V_{on}) was modest at 3.2 V and the peak power efficiency (PE_{max}) was 28.7 lm W^{-1}. Although the peak performance of the device establishes the naphthalene-acceptor based design as an effective strategy for designing efficient OLEDs, the severe efficiency roll-off at higher luminance values indicates that there remains significant effort to improve the device performance further.

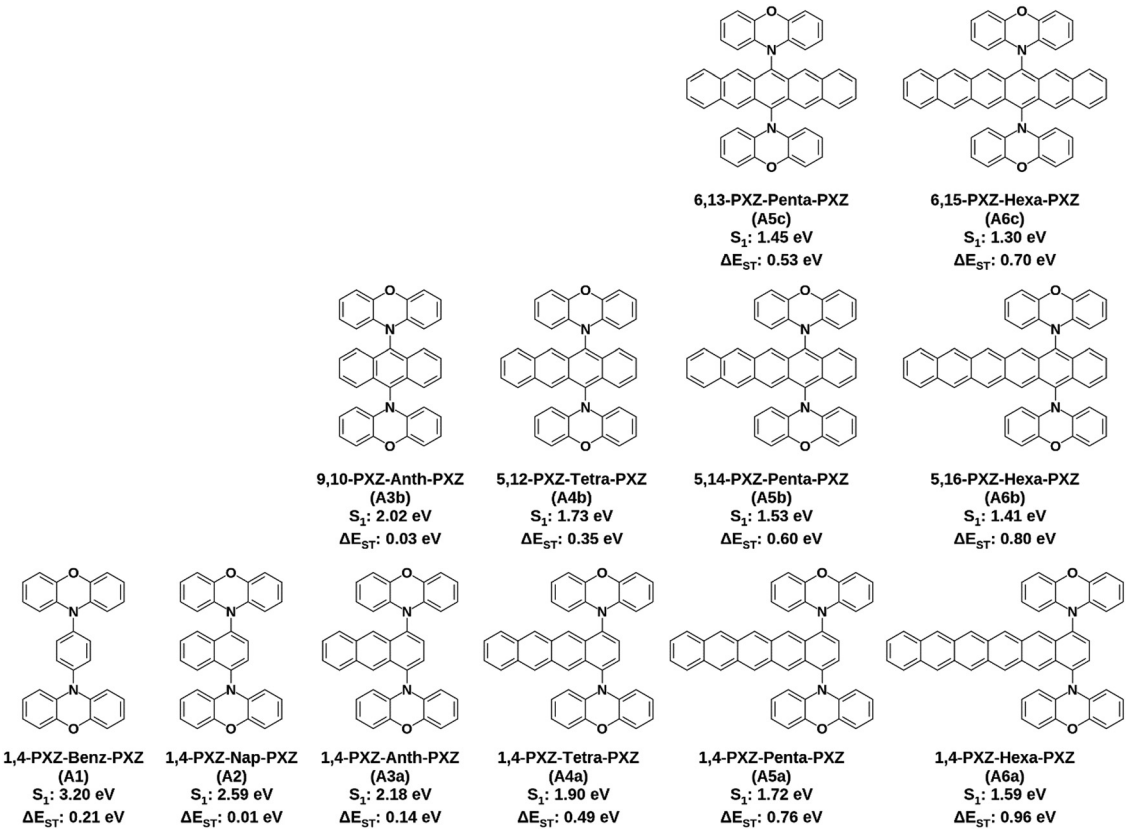

Fig. 12 Structures, names, S_1 energies and ΔE_{ST} of the 12 emitters investigated, calculated at the PBE0-D3(BJ)/6-31G(d,p) level of theory in the gas phase.

Theoretical investigation of larger acenes

Considering the results obtained from the device based on **1,4-PXZ-Nap-PXZ** we next chose to investigate *in silico* whether an even larger acene acting as an electron-acceptor would also yield compounds likely to show TADF. To this end we designed an additional 11 molecules based on the PXZ-*acene*-PXZ structure where *acene* is one of either benzene, anthracene, tetracene, pentacene or hexacene and the two donors were placed in all symmetrical combinations on either side of the ring system (Fig. 12). The results from this computational study are shown in Fig. 13 and 14. As the size of the acene part of the compound is increased, the energy of the LUMO is substantially stabilized because the LUMO is localized to the acene moiety (Fig. 13). Meanwhile, the HOMO is almost unchanged since it remains largely localized to the phenoxazine units, except in the hexacene derivatives where the HOMO is instead localized to the acene (the HOMO−1 is now localized on the phenoxazine unit), which is accompanied by a minor destabilization effect. Between the different substitution patterns, there is a simultaneous

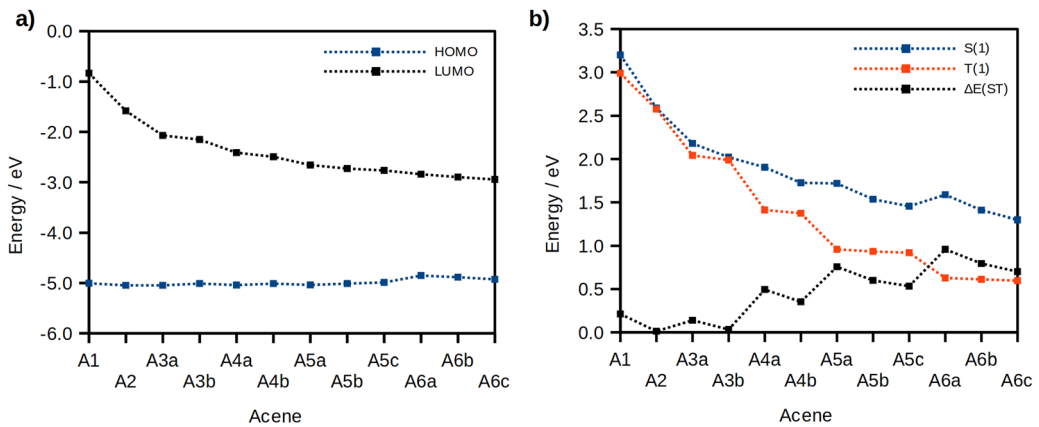

Fig. 13 (a) Computed HOMO and LUMO energies and (b) S_1 and T_1 energies calculated at the PBE0-D3(BJ)/6-31G(d,p) level of theory in the gas phase.

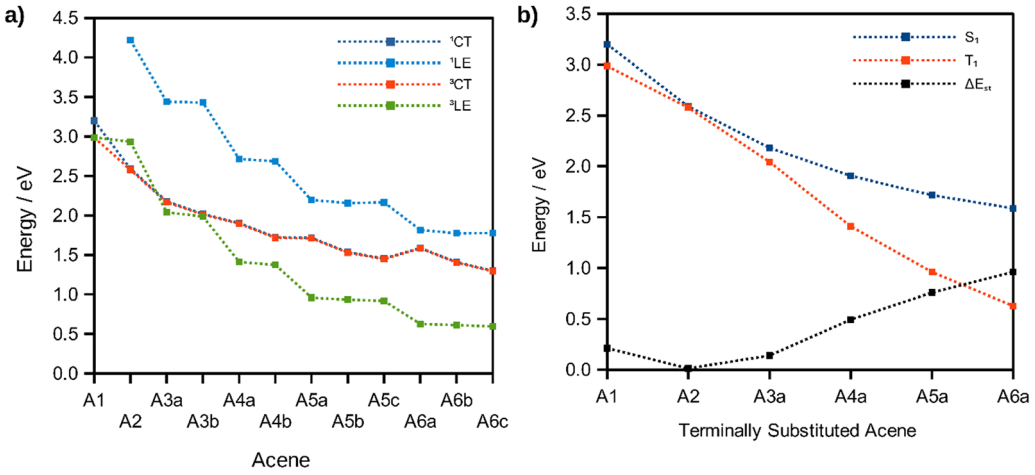

Fig. 14 (a) The computed lowest energy locally excited singlet (^{1}LE), locally excited triplet (^{3}LE), charge-transfer singlet (^{1}CT) and charge-transfer triplet (^{3}CT), and (b) the computed S_1 and T_1 energies (as shown in Fig. 13b) of the centrally substituted acenes only, calculated at the PBE0-D3(BJ)/6-31G(d,p) level of theory in the gas phase.

stabilization of the LUMO and a slight destabilization of the HOMO as the phenoxazines are placed closer to the centre, but the change in the LUMO is greater, resulting in a decrease of the electronic band gap. Hexacene again acts as an exception, with both the HOMO and LUMO stabilized simultaneously as the donors retreat from the periphery of the acene. In all cases, the stabilization of the LUMO is associated with a stronger electronic interaction between the LUMO of the phenoxazine and the acene when the donors are placed near the centre of the acene core. A small coefficient of the LUMO density is therefore located on the phenoxazine donor (Fig. S1, ESI†) and this coefficient is greater in the centrally substituted case, thus leading to a stronger stabilization of the LUMO. This stronger electronic interaction is a consequence of the larger LUMO density near the centre of the acene core as opposed to the outer rings.

Across the entire series, the S_1 state retains a large CT character and is mostly described by a HOMO to LUMO transition, except in the hexacene derivatives where it is best described by a HOMO−1 to LUMO transition (Table 5). Correspondingly, a significant red-shift in S_1 is observed as the acene size increases due to the increasing stabilization of the LUMO (Fig. 13b), with **1,4-PXZ-Hexa-PXZ** (S_1 = 1.59 eV) and **6,15-PXZ-Hexa-PXZ** (S_1 = 1.30 eV) exhibiting the smallest S_1 energies for their respective substitution patterns. We also observed that the magnitude of the S_1 energy red-shift is larger when the donors are placed closer to the centre of the acene core, consistent with the trend in the electronic band gap, and this effect is more prominent in the larger acenes. As such, the S_1 of the terminally substituted hexacene derivative (**1,4-PXZ-Hexa-PXZ**, **A6a**, S_1 = 1.59 eV) is higher in energy than that of the centrally substituted pentacene derivative (**6,13-PXZ-Pent-PXZ**, **A5a**, S_1 = 1.45).

The evolution of the T_1 energy differs significantly from that of the S_1 because of the competing contributions from states possessing locally excited (^{3}LE) and charge-transfer (^{3}CT) character (Fig. 14a). For the phenyl and naphthalene derivatives, the T_1 state is predominantly CT in character (Table 5). However, starting from the anthracene derivative, the locally excited triplet state localized on the acene core becomes more stabilised than the ^{3}CT. This arises because the energy ordering of the triplet states of donor–acceptor compounds is ruled by the

Table 5 Principal transitions and resulting nature of the S_1 and T_1 excited states

Emitter	S_1 principal transitions (probability/%)	S_1 nature[a]	T_1 principal transitions (probability/%)	T_1 nature[a]
A1	HOMO → LUMO (99)	CT	HOMO−1 → LUMO+2 (37) HOMO → LUMO+3 (25) HOMO → LUMO+1 (30)	HLCT
A2	HOMO → LUMO (99)	CT	HOMO → LUMO (99)	CT
A3a	HOMO → LUMO (99)	CT	HOMO−2 → LUMO (94)	LE
A3b	HOMO → LUMO (99)	CT	HOMO−2 → LUMO (95)	LE
A4a	HOMO → LUMO (98)	CT	HOMO−2 → LUMO (94)	LE
A4b	HOMO → LUMO (99)	CT	HOMO−2 → LUMO (95)	LE
A5a	HOMO → LUMO (98)	CT	HOMO−2 → LUMO (94)	LE
A5b	HOMO → LUMO (99)	CT	HOMO−2 → LUMO (95)	LE
A5c	HOMO → LUMO (99)	CT	HOMO−2 → LUMO (95)	LE
A6a	HOMO−1 → LUMO (97)	CT	HOMO → LUMO (94)	LE
A6b	HOMO−1 → LUMO (98)	CT	HOMO → LUMO (94)	LE
A6c	HOMO−1 → LUMO (99)	CT	HOMO → LUMO (95)	LE

[a] CT = charge-transfer, HLCT = hybrid local and charge transfer, LE = local excitation.

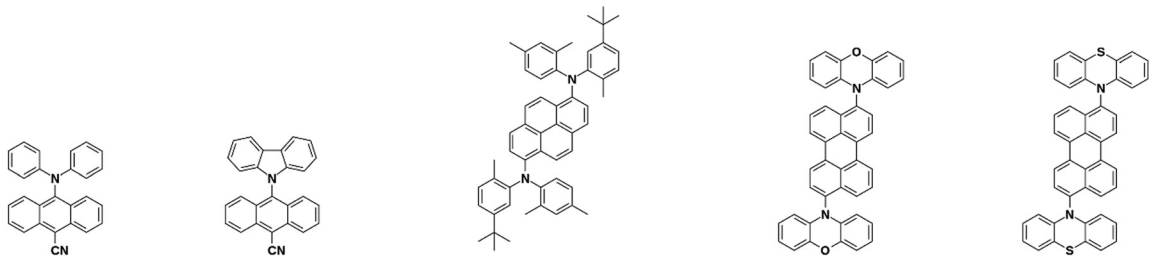

DPAAnCN
J. Mater. Chem. C, **2020**, *8*, 3773
Mechanism: hot-exciton,
ΔE_{ST}: 0.74 eV[a], EQE_{max}: 6.0%

CzAnCN
J. Mater. Chem. C, **2020**, *8*, 3773
Mechanism: hot-exciton,
ΔE_{ST}: 0.75 eV[a], EQE_{max}: 4.0%

3Me-1Bu-TPPDA
ACS Appl. Mater. Interfaces, **2018**, *10*, 30022 - 30028
Mechanism: fluorescence,[b]
ΔE_{ST}: 0.84 eV[c], EQE_{max}: 9.3%

Pery-2PXZ
J. Mater. Chem. C, **2022**, *10*, 9758
Mechanism: triplet-triplet-annihilation,
ΔE_{ST}: 0.65 eV[d], EQE_{max}: NR

Pery-2PTZ
J. Mater. Chem. C, **2022**, *10*, 9758
Mechanism: triplet-triplet-annihilation,
ΔE_{ST}: 0.62 eV[d], EQE_{max}: NR

Fig. 15 The structure, emission mechanism and ΔE_{ST} of emitters based on larger acenes reported in the literature. [a] Computed at the TDA-PBE0-D3(BJ)/6-31G(d,p) level. [b] As stated by the authors.[28] [c] The difference in energy of the fluorescence peak measured in toluene at room temperature and the phosphorescence peak measured in toluene at 77 K with a 30 ms delay. [d] The difference in energy of the onset of fluorescence measured in DCM at room temperature and the T_1 state calculated at the TD-DFT-B3LYP/6-31G level.

interplay between the magnitude of the electronic interaction between the electron-donating and the electron-accepting units, which tends to stabilize the ^{3}CT, and the exchange interaction which favours the ^{3}LE as the lowest triplet energy state. As a result, the energy of the T_1 state decreases significantly with increasing ring size but is essentially invariant across different substitution patterns where the acene acceptor remains constant since the T_1 transition is essentially localized on the acene bridge. The corresponding locally-excited singlet state (^{1}LE), meanwhile, remains higher in energy than the charge-transfer state (^{1}CT) because the exchange interaction energy does not affect singlets.

As a direct consequence, we observed a sizeable decrease in ΔE_{ST} from 0.21 to 0.01 eV for the phenyl and naphthalene derivatives respectively, explained by the larger delocalization of the LUMO, which further strengthens the CT character of both S_1 and T_1. However, starting from the anthracene derivatives, the disproportionate stabilisation of the locally excited triplet compared to the charge-transfer singlet results in a steep increase in ΔE_{ST} (Fig. 14b), up to a maximum of 0.96 eV in **1,4-PXZ-Nap-PXZ** (**A6a**). Conversely, there is a stabilization of the ^{1}CT as the donor position is moved from the terminus of the acene towards the centre, while the ^{3}LE remains constant, resulting in a sizeable decrease in ΔE_{ST}, and as such the centrally substituted hexacene derivative (**6,15-PXZ-Hex-PXZ**, **A6c**) has a noticeably smaller ΔE_{ST} of 0.70 eV.

With these results in hand, it becomes clear that of all the acenes evaluated naphthalene is the most ideally suited to act as an acceptor for developing TADF emitters. The ΔE_{ST} of the centrally substituted anthracene derivative was also minimized, but the inversion of the ^{3}LE and ^{3}CT states means this is not guaranteed for other donors, and any blue-shifting of the emission is likely to be accompanied by an increase in ΔE_{ST}. In particular, acenes larger than anthracene will likely possess a ΔE_{ST} that is too large for TADF, unless either the S_1 energy is substantially stabilized and/or the T_1 state is sufficiently destabilised. This observation is corroborated by recent reports in the literature of donor–acceptor emitters containing larger acenes such as anthracene, pyrene and perylene (Fig. 15). The emitters **DPAAnCN** and **CzAnCN** have been previously reported by our group[26] and consist of a cyanoanthracene core centrally substituted with diphenylamine and carbazole, respectively. Similarly, the emitters **Pery-2PXZ** and **Pery-2PTZ**, reported by Li *et al.*,[27] contain a perylene core substituted with either phenoxazine or phenothiazine as donor groups, respectively. Each of these four emitters has a large ΔE_{ST} of >0.6 eV (in **DPAAnCN** and **CzAnCN** this ΔE_{ST} is reported from TD-DFT,[26] while in **Pery-2PXZ** and **Pery-2PTZ** it is calculated by the authors from the difference in energy of the TD-DFT-calculated T_1 energy and the measured onset of fluorescence[27]), which is too large for efficient TADF. Instead, these emitters operate *via* alternative triplet harvesting mechanisms. In the case of **DPAAnCN** and **CzAnCN**, the exciton harvesting mechanism was hypothesised to employ a 'hot-exciton' channel,[26] while the perylene derivatives **Pery-2PXZ** and **Pery-2PTZ** were shown to operate *via* triplet–triplet-annihilation (TTA).[27] Devices based on these hot-exciton emitters achieved appreciable EQE_{max} of 6.0% and 4.0% for the OLEDs with **DPAAnCN** and **CzAnCN**, respectively,[26] while no devices were fabricated based on the TTA emitters. Finally, a family of pyrene derived emitters were reported by Park *et al.*,[28] exemplified by **3Me-1Bu-TPPDA**, which possesses a very large ΔE_{ST} of 0.84 eV and was reported to be fluorescent. However, it should be noted that an OLED based on this emitter achieved an EQE_{max} of 9.3%, in excess of the 5% limit for fluorescent devices. This strongly suggests that a triplet-harvesting mechanism is operational in the device.

Conclusions

Herein, we have conducted a computational screen of 36 naphthalene-containing emitters to evaluate their promise as TADF emitters. Three of the compounds, **2-PXZ-Nap**, **1-PXZ-Nap** and **1,4-PXZ-Nap-PXZ**, were then identified as being the most promising and were subsequently synthesised. The photophysical properties of these emitters in toluene and DCM solution and doped films in PMMA and mCP were measured. A high

photoluminescence quantum yield of 48% and evidence of TADF were recorded for **1,4-PXZ-Nap-PXZ** as a 20 wt% doped film in mCP. An OLED employing this emitter demonstrated an EQE_{max} = 10.5%, PE_{max} = 28.7 lm W^{-1} with green emission (λ_{EL} = 505 nm). This is, to the best of our knowledge, the first reported OLED utilising a TADF emitter in which naphthalene alone acts as the acceptor moiety. This initial study clearly demonstrates the potential of the acene acceptor design for the development of TADF emitters. Finally, a comprehensive computational study has been presented to demonstrate why naphthalene alone of the linear acenes is suitable for constructing donor-acene-donor TADF emitters of this type.

Conflicts of interest

There are no conflicts to declare.

Acknowledgements

Some computations were performed using resources kindly provided by the University of Mons (UMONS), supported by the Belgian National Fund for Scientific Research (FRS-FNRS). These computational resources were provided by the Consortium des Équipements de Calcul Intensif (CÉCI) funded by F. R. S.-FNRS under Grant 2.5020.11. Y. O. acknowledges funding by the Fonds de la Recherche Scientifique-FNRS under Grant no. F.4534.21 (MIS-IMAGINE).

References

1 M. Y. Wong and E. Zysman-Colman, *Adv. Mater.*, 2017, **29**, 1605444.
2 S. Reineke and M. A. Baldo, *Phys. Status Solidi A*, 2012, **209**, 2341–2353.
3 T. D. Schmidt, M. Flämmich, B. J. Scholz, D. Michaelis, C. Mayr, N. Danz and W. Brütting, *Org. Photonics V*, 2012, **8435**, 843513.
4 F. Tenopala-Carmona, O. S. Lee, E. Crovini, A. M. Neferu, C. Murawski, Y. Olivier, E. Zysman-Colman and M. C. Gather, *Adv. Mater.*, 2021, **33**, 2100677.
5 P. Nuss and M. J. Eckelman, *PLoS One*, 2014, **9**, e101298.
6 G. M. Mudd, *Ore Geol. Rev.*, 2012, **46**, 106–117.
7 H. Uoyama, K. Goushi, K. Shizu, H. Nomura and C. Adachi, *Nature*, 2012, **492**, 234–238.
8 D. Hall, J. C. Sancho-García, A. Pershin, D. Beljonne, E. Zysman-Colman and Y. Olivier, *J. Phys. Chem. A*, 2023, **127**, 4743–4757.
9 L. Zhu, H. Zhang, X. Peng, M. Zhang, F. Zhou, S. Chen, J. Song, J. Qu and W. Y. Wong, *Dyes Pigm.*, 2021, **194**, 109627.
10 J. Wang, J. Liang, Y. Xu, B. Liang, J. Wei, C. Li, X. Mu, K. Ye and Y. Wang, *J. Phys. Chem. Lett.*, 2019, **10**, 5983–5988.
11 S. Paredis, T. Cardeynaels, J. Deckers, A. Danos, D. Vanderzande, A. P. Monkman, B. R. Champagne and W. Maes, *J. Mater. Chem. C*, 2022, **10**, 4775–4784.
12 Y. Li, J.-Y. Liu, Y.-D. Zhao and Y.-C. Cao, *Mater. Today*, 2017, **20**, 258–266.
13 H. Park, J. Lee, I. Kang, H. Y. Chu, J. I. Lee, S. K. Kwon and Y. H. Kim, *J. Mater. Chem.*, 2012, **22**, 2695–2700.
14 M. Mahmoudi, J. Keruckas, D. Volyniuk, V. Andrulevičienė, R. Keruckienė, E. Narbutaitis, Y. C. Chao, M. Rutkis and J. V. Grazulevicius, *Dyes Pigm.*, 2022, **197**, 109868.
15 Q. Sun, X. Zhang, S. Banerjee, P. Bao, M. Barbry, N. S. Blunt, N. A. Bogdanov, G. H. Booth, J. Chen, Z.-H. Cui, J. J. Eriksen, Y. Gao, S. Guo, J. Hermann, M. R. Hermes, K. Koh, P. Koval, S. Lehtola, Z. Li, J. Liu, N. Mardirossian, J. D. McClain, M. Motta, B. Mussard, H. Q. Pham, A. Pulkin, W. Purwanto, P. J. Robinson, E. Ronca, E. R. Sayfutyarova, M. Scheurer, H. F. Schurkus, J. E. T. Smith, C. Sun, S.-N. Sun, S. Upadhyay, L. K. Wagner, X. Wang, A. White, J. D. Whitfield, M. J. Williamson, S. Wouters, J. Yang, J. M. Yu, T. Zhu, T. C. Berkelbach, S. Sharma, A. Y. Sokolov and G. K.-L. Chan, *J. Chem. Phys.*, 2020, **153**, 024109.
16 Y. Olivier, B. Yurash, L. Muccioli, G. D'Avino, O. Mikhnenko, J. C. Sancho-García, C. Adachi, T.-Q. Nguyen and D. Beljonne, *Phys. Rev. Mater.*, 2017, **1**, 075602.
17 W. Zeng, S. Gong, C. Zhong and C. Yang, *J. Phys. Chem. C*, 2019, **123**, 10081–10086.
18 Y. Olivier, M. Moral, L. Muccioli and J.-C. Sancho-García, *J. Mater. Chem. C*, 2017, **5**, 5718–5729.
19 N. G. Connelly and W. E. Geiger, *Chem. Rev.*, 1996, **96**, 877–910.
20 G. Grabner, K. Rechthaler, B. Mayer, G. Köhler and K. Rotkiewicz, *J. Phys. Chem. A*, 2000, **104**, 1365–1376.
21 B. Sk, S. Sharma, A. James, S. Kundu and A. Patra, *J. Mater. Chem. C*, 2020, **8**, 12943–12950.
22 G. A. Crosby and J. N. Demas, *J. Phys. Chem.*, 1971, **75**, 991–1024.
23 T.-Y. Hwang, Y. Choi, Y. Song, N. S. A. Eom, S. Kim, H.-B. Cho, N. V. Myung and Y.-H. Choa, *J. Mater. Chem. C*, 2018, **6**, 972–979.
24 P. Sudhakar, A. Kumar Gupta, D. B. Cordes and E. Zysman-Colman, *Chem. Sci.*, 2024, **15**, 545–554.
25 C. Si, Y.-N. Hu, D. Sun, K. Wang, X.-H. Zhang and E. Zysman-Colman, *J. Mater. Chem. C*, 2023, **11**, 12174–12184.
26 N. Sharma, M. Y. Wong, D. Hall, E. Spuling, F. Tenopala-Carmona, A. Privitera, G. Copley, D. B. Cordes, A. M. Z. Slawin, C. Murawski, M. C. Gather, D. Beljonne, Y. Olivier, I. D. W. Samuel and E. Zysman-Colman, *J. Mater. Chem. C*, 2020, **8**, 3773–3783.
27 M. Imran, J. Pang, J. Zhao and M.-D. Li, *J. Mater. Chem. C*, 2022, **10**, 9758–9772.
28 H. Jung, S. Kang, H. Lee, Y. J. Yu, J. H. Jeong, J. Song, Y. Jeon and J. Park, *ACS Appl. Mater. Interfaces*, 2018, **10**, 30022–30028.

